Deposition of Sodium Metal at the Copper-NaSICON Interface for Reservoir-Free Solid-State Sodium Batteries

Till Ortmann, Till Fuchs, Janis K. Eckhardt, Ziming Ding, Qianli Ma, Frank Tietz, Christian Kübel, Marcus Rohnke,* and Jürgen Janek*

"Anode-free" solid-state battery concepts are explored extensively as they promise a higher energy density with less material consumption and simple anode processing. Here, the homogeneous and uniform electrochemical deposition of alkali metal at the interface between current collector and solid electrolyte plays the central role to form a metal anode within the first cycle. While the cathodic deposition of lithium has been studied intensively, knowledge on sodium deposition is scarce. In this work, dense and uniform sodium layers of several microns thickness are deposited at the $Cu|Na_{3.4}Zr_2Si_{2.4}P_{0.6}O_{12}$ interface with high reproducibility. At current densities of ≈ 1 mA•cm^{-2}, relatively uniform coverage is achieved underneath the current collector, as shown by electrochemical impedance spectroscopy and 3D confocal microscopy. In contrast, only slight variations of the coverage are observed at different stack pressures. Early stages of the sodium metal growth are analyzed by in situ transmission electron microscopy revealing oriented growth of sodium. The results demonstrate that reservoir-free ("anode-free") sodium-based batteries are feasible and may stimulate further research efforts in sodium-based solid-state batteries.

1. Introduction

Sodium solid-state batteries gain increasing research interest following the fast rise of sodium-ion batteries because of the potential use of sodium metal as anode material in combination with a solid electrolyte (SE) separator.[1–4] Sodium metal has a high specific capacity ($q_{th} = 1165$ mAh•g^{-1}) and low standard potential ($E_H = -2.71$ V vs standard hydrogen electrode), which can significantly increase energy and power density compared to carbon-based anodes.[5,6] Achieving a reversible sodium metal anode, however, poses several challenges – including a clean interface with sufficient interfacial contact, and an electrochemically stable interface with a solid electrolyte.[7] In addition, the high reactivity of sodium metal requires inert atmosphere conditions during processing, which increases the production costs of sodium solid-state batteries.[8,9]

"Zero-excess" or "reservoir-free" cell concepts, also often called "anode-free", could be a possible solution to these challenges and are encountering a rapidly growing research activity.[9–12] Most cathode active materials are synthesized in the discharged (sodiated or pre-sodiated) state.[13] During the first charge of a cell, sodium ions are extracted from the cathode active material and electrodeposited on a current collector (CC) (e.g., aluminum or copper), forming the sodium metal anode in situ.[14,15] This further increases the volumetric

T. Ortmann, T. Fuchs, J. K. Eckhardt, M. Rohnke, J. Janek
Institute for Physical Chemistry
Justus Liebig University Giessen
35392 Giessen, Germany
E-mail: marcus.rohnke@phys.chemie.uni-giessen.de;
juergen.janek@phys.chemie.uni-giessen.de
T. Ortmann, T. Fuchs, J. K. Eckhardt, M. Rohnke, J. Janek
Center for Materials Research (ZfM)
Justus Liebig University Giessen
35392 Giessen, Germany

Z. Ding, C. Kübel
Department of Materials & Earth Sciences
Technische Universität Darmstadt
64289 Darmstadt, Germany

Z. Ding, C. Kübel
Institute of Nanotechnology (INT) and Helmholtz Institute Ulm (HIU)
Karlsruhe Institute of Technology (KIT)
76344 Eggenstein-Leopoldshafen, Germany

Q. Ma, F. Tietz
Institute of Energy and Climate Research
Materials Synthesis and Processing (IEK-1)
Forschungszentrum Jülich GmbH
52425 Jülich, Germany

C. Kübel
Karlsruhe Nano Micro Facility (KNMF)
Karlsruhe Institute of Technology (KIT)
76344 Eggenstein-Leopoldshafen, Germany

**ADVANCED
SCIENCE NEWS**

www.advancedsciencenews.com

**ADVANCED
ENERGY
MATERIALS**

www.advenergymat.de

and gravimetric energy density of reservoir-free cells compared to conventional Na|SE|Cathode battery architectures including a sodium foil. It also reduces production costs and energy consumption during cell manufacture by avoiding the need to produce and process sodium metal foils or layers.[9]

However, the successful operation of reservoir-free cells also poses a number of challenges. For instance, the uniform and reversible metal deposition on the CC plays a key role.[9] While the influence of (modified) CC material,[14–18] deposition protocol,[19] external stack pressure,[13] and electrolyte composition[20,21] on the cathodic deposition of sodium at a CC|liquid electrolyte interface have been studied, less is known about the deposition at CC|SE interface.[22]

The cathodic deposition of a parent metal on a SE has early been studied by silver deposition on AgX (X = Cl, Br) revealing a preferential nucleation at surface defects like surface scratches.[23–25] As shown by microelectrode experiments, the silver morphology strongly depends on the applied current density.[24] Later, the cathodic deposition of lithium at a CC|LiPON interface was systematically investigated by Motoyama et al.[26–28] By increasing the current density j_{app}, a growing number of lithium nuclei N_{Li} are formed per interface area, leading to more uniform deposition, while increasing the temperature decreases N_{Li} and affects the lithium morphology.[27] Since LiPON is an amorphous SE, lithium deposition was also studied at CC|$Li_{6+x}La_3Zr_{2-x}M_xO_{12}$ (with M = Al, Ta) (LLZO) interfaces to evaluate the influence of grain boundaries and surface defects. As with LiPON, N_{Li} increases with higher j_{app}, with preferential nucleation observed at surface defects.[12,29,30] Recently, lithium deposition under a CC has been investigated in bulk solid-state batteries, showing the importance of the interfacial adhesion between CC and SE on the nucleation and growth behavior.[31] Moreover, the stack pressure was shown to affect the lateral growth behavior of lithium at the Cu|LLZO interface.[32] The operating principle of solid-state reservoir-free cells has already been demonstrated for lithium by electrodeposition of reasonable capacities of 5 mAh•cm^{-2} that corresponds to a layer thickness $d_{Li} \approx 24$ µm.[31,33–35] For the same capacity, the layer thickness would nearly double in the case of sodium ($d_{Na} \approx 44$ µm), due to the higher molar volume of sodium metal.

Based on the low interface-related resistance and the formation of a kinetically stabilized interphase in contact with sodium, $Na_{3.4}Zr_2Si_{2.4}P_{0.6}O_{12}$ (NZSP) is an ideal SE to study the deposition of sodium at a CC|SE interface.[36–39] Copper was chosen as the current collector material because of its ease of processing on a laboratory scale and to avoid alloying effects with sodium. The nucleation and growth of sodium at the interface between copper and NZSP has not yet been studied and a detailed analysis of the evolution of the interfacial morphology at different deposition conditions is lacking in the literature.

In this study, we investigate the deposition of sodium at a Cu|NZSP interface at different current densities and stack pressures. Time-dependent impedance spectroscopy is used to analyze the morphological evolution during deposition, followed by 3D profiling of the copper current collector by confocal microscopy. An increase in current density results in more uniform sodium deposition. In contrast, no significant change in the sodium coverage is observed with increasing stack pressure. The growth of dense and uniform sodium layers between copper

and NZSP is shown by cross-sections prepared via focused ion beam-scanning electron microscopy (FIB-SEM). In addition, island and whisker growth are observed, leading to the formation of gaps between copper and NZSP. In situ transmission electron microscopy (TEM) further reveals the growth of sodium whiskers with a faceted microstructure.

2. Results and Discussion

For the characterization of sodium deposition, Cu|NZSP|Na$_{id}$ cells with a copper layer thickness of 5 µm were assembled. An ideal sodium counter electrode (Na$_{id}$) acts as a sodium reservoir and quasi-reference electrode. A quasi-reference electrode is an electrode that shows no significant interfacial polarization and has a stable potential despite low current load, as demonstrated by Krauskopf et al.[36,40] Two series of measurements were performed to investigate the influence of current density j_{app} and external pressure p on sodium deposition. While a constant pressure of 2 MPa was used for the current density series, a constant current of 200 µA•cm^{-2} was used for the stack pressure series. An overview of the cell preparation and the selected j_{app} and p is shown in Figure S1 (Supporting Information).

2.1. Potential Profiles

Figure 1a,b shows the potential profiles of the performed current density and stack pressure series. The parameters (j_{app} and p) of the two measurement series were chosen such that the measurement at 200 µA•cm^{-2} and 2 MPa (light green curve) is included in both series (see Figure S1b, Supporting Information). Starting from an open circuit voltage of 1.0–2.1 V, all voltage profiles show a strong initial drop below the standard potential of sodium $E_H(Na^+/Na)$ at the beginning of the deposition. Afterward, the voltage generally increases and turns into a plateau, which remains always below $E_H(Na^+/Na)$. The initial potential drop can be attributed to the nucleation of sodium at the current collector and the subsequent plateau at higher potentials to the growth of the formed nuclei.[26,41,42]

The onsets of sodium deposition for the current density and stack pressure series are shown magnified in Figure 1c,d. The voltage profiles are slightly shifted along the x-axis to give a better overview of the individual curves. With increasing j_{app}, less fluctuations are observed in the potential curves during the first deposition step. While at atmospheric pressure (labeled with "ATM") a "smoother" potential profile is observed during the initial growth, slight fluctuations are present when a stack pressure is applied.

Fluctuations were also reported during the initial growth of lithium at a Cu|LLZO interface, while none are observed during electrodeposition from liquid electrolytes or thin film current collectors in contact with a SE.[12,26,27,32,42] A relationship between the fluctuations and the interfacial morphology, including the delamination of the copper current collector, is therefore likely.[32] Thus, for the Cu|NZSP interface the fluctuations may be due to changes in the interfacial morphology, including possible damage of the SE near the Na|NZSP interface. However, it is unclear why this phenomenon preferentially occurs at low current densities and stack pressures.
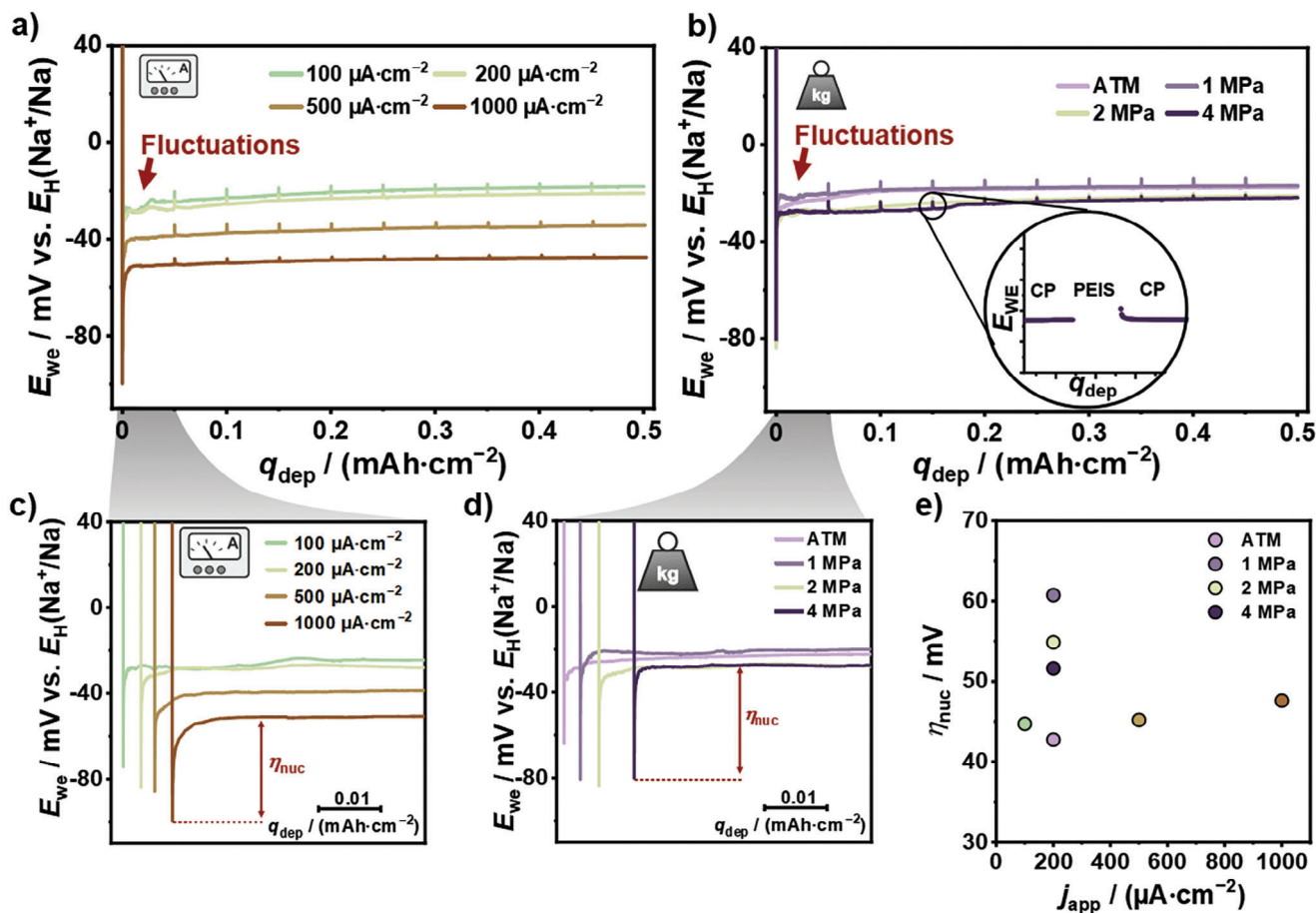
Figure 1. Potential profile of cathodic deposition of sodium at a Cu|NZSP interface at various a) current densities and b) stack pressures. A pressure of 2 MPa was applied for measurements at different current densities. Depositions at atmospheric pressures (ATM) and different stack pressures were performed at a current density of j_{app} = 200 µA·cm^{-2}. The pictogram insert in (a) and (b) indicates the individual measurement series. Measurements were conducted at 25 °C and a sodium amount corresponding to an areal charge q_{dep} of 0.5 mAh·cm^{-2} was deposited at the Cu|NZSP interface in all cells. Impedance spectra were recorded after each 0.05 mAh·cm^{-2} deposition step to characterize the evolution of the Cu|NZSP interface. The impedance measurements result in the small and regular dips in the potential profile for each cell. The initial drop in the potential profile for both series is depicted at higher magnification for c) current density and d) stack pressure series to visualize the nucleation overpotential η_{nuc}. The potential curves were slightly shifted along the x-axis to give a better overview of their individual course. The corresponding scale is given by the black bar. The determined η_{nuc} for the current densities (green and brown points) and stack pressure series are shown in e). For the determination of η_{nuc}, the difference between the voltage drop and the average voltage plateau in the range between 0.05 and 0.25 mAh·cm^{-2} was extracted from the graphs.

The nucleation overpotential η_{nuc} was calculated for all measurements by the difference between the initial potential drop and the potential plateau (see Figure 1c,d).[41] The values of η_{nuc} are summarized in Figure 1e. For both series of measurements, only small changes in the range of a few mV were observed for η_{nuc}, which does not allow an identification of a clear trend. In the case of the nucleation of lithium at the Cu|LiPON interface, a significant increase in η_{nuc} was observed at higher j_{app}, especially at elevated temperatures (60 to 100°C).[27] In the case of sodium nucleation, it might be possible to identify a trend of η_{nuc} by expanding the parameter window, which will be part of future studies.

After nucleation and early growth (q_{dep} > 0.05 µAh·cm^{-2}), a constant potential for all measurements is observed, indicating a stable growth of sodium at the Cu|NZSP interface. However, considering the current density series (green to brown curves), doubling of the deposition potential is usually expected by dou-

bling j_{app}, which is not observed. This is due to the dependence of the potential on the total resistance of the cell. This resistance varies depending on the interfacial contact between sodium and NZSP and volume of the SE actively involved in transport. This also explains why different growth overpotentials η_{growth} are obtained for the same j_{app}. The non-linear behavior shows that the nucleation and growth is influenced by the deposition conditions. A more detailed analysis of the individual changes is possible by electrochemical impedance spectroscopy and is discussed in the following section.

2.2. Electrochemical Impedance Spectroscopy

Electrochemical impedance spectroscopy enables the identification and quantification of individual processes such as ionic transport, interface-related processes or chemical degradation in
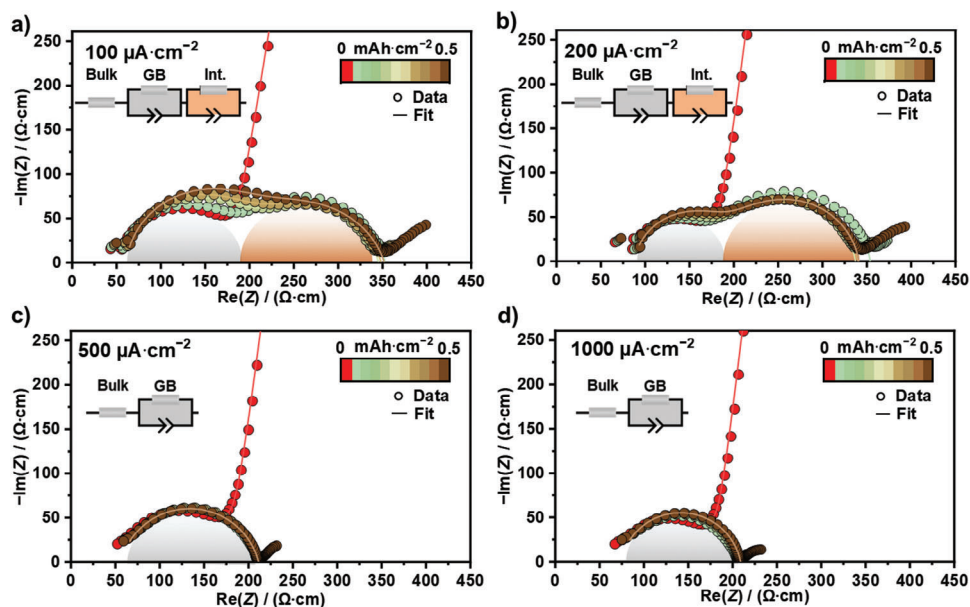
Figure 2. Development of the impedance spectra during cathodic deposition of sodium at the Cu|NZSP interface at various current densities. All impedance data are normalized with respect to the cell constant instead of the electrode area. The grain boundary transport contribution is highlighted by a gray area while the interface-related contribution is indicated by an orange background. The inserted equivalent circuit diagram was used to fit the impedance data except for the pristine cells (red dots). Here, the blocking behavior of the copper electrode was fitted by a Q-instead of an RQ-element. The evolution of the extracted fitting parameters R_{SE}, R_{Int}, and C_{Int} with progressing sodium deposition is shown in Figure 3.

electrochemical cells.[43] Apart from microscopic transport processes such as transport across grain boundaries or charge transfer at phase boundaries, additional non-microscopic transport contributions can occur in impedance spectra such as geometric current constriction. The latter results from insufficient physical contact at the alkali metal|SE interface and shows the same signature in the impedance spectrum as a true migration process, i.e., a semicircle in the Nyquist diagram.[44] This is due to the dynamic nature of the conduction behavior of pores at the interface in the measured frequency range. At low excitation frequencies, ionic charge transport is blocked by an insulating gap at the metal|SE interface, while at higher frequencies, charge transport can occur across the gap by a dielectric displacement current.[44] As a result, the SE volume actively involved in transport is reduced in the direct current range, leading to the increase in the impedance. In particular, for the Li|LLZO and Na|NZSP interfaces, it has been demonstrated that the interface-related impedance contribution R_{Int} is dominated by this geometric phenomenon.[36,40,45]

Note that current constriction is a purely geometric effect and is given by the morphology of the interface. A systematic investigation of the influence of contact area, contact area distribution, electrode area, and gap height on the current constriction phenomenon was reported in detail by Eckhardt et al.[44–46] For example, a decrease of the contact area leads to an increase of the current constriction resistance R_{cstr}, while a finer spatial distribution of contact at constant contact area would decrease R_{cstr}. Furthermore, the constriction capacity C_{cstr} is strongly affected by the interfacial morphology, meaning the shape of gaps (height and contact area). Thus, time-resolved electrochemical impedance spectroscopy is a suitable tool to qualitatively monitor the evolution

of the interfacial morphology during sodium deposition at the Cu|NZSP interface.

However, to unambiguously monitor changes at the Cu|NZSP interface, changes at the counter electrode|SE interface must be avoided. As shown in a previous work, an ideal sodium electrode Na_{id} does not show any interfacial polarization in contact with NZSP and thus no interface-related contribution in the impedance spectrum.[36] Moreover, a Na_{id} electrode can still serve as a quasi-reference electrode even when small amounts (<0.5 mAh•cm^{-2}) of sodium are anodically dissolved at a Na_{id}|NZSP interface.[36] Thus, changes of the interface-related impedance in the performed measurement series can be assigned to the Cu|NZSP interface, whereby $R_{Int} \approx R_{cstr}$.

For both measurement series, cells were characterized in intervals of 0.05 mAh•cm^{-2}, as can be seen by the short breaks in the potential profiles (Figure 1a,b). A detailed explanation of the impedance data is given based on the current density series shown in **Figure 2**. This is followed by a discussion of the stack pressure series. For better comparison, the impedances of the different samples were normalized to the cell constant instead of the working electrode area. This is necessary because the cells have slightly different thicknesses due to the polishing process. Thus, all resistances are given in Ω•cm instead of Ω•cm^2, while capacities are given in nF•cm^{-1} instead of nF•cm^{-2}.

2.2.1. Current Density Series

For pristine cells (red data points), only one semicircle in the high-frequency range is observed in the Nyquist plot with
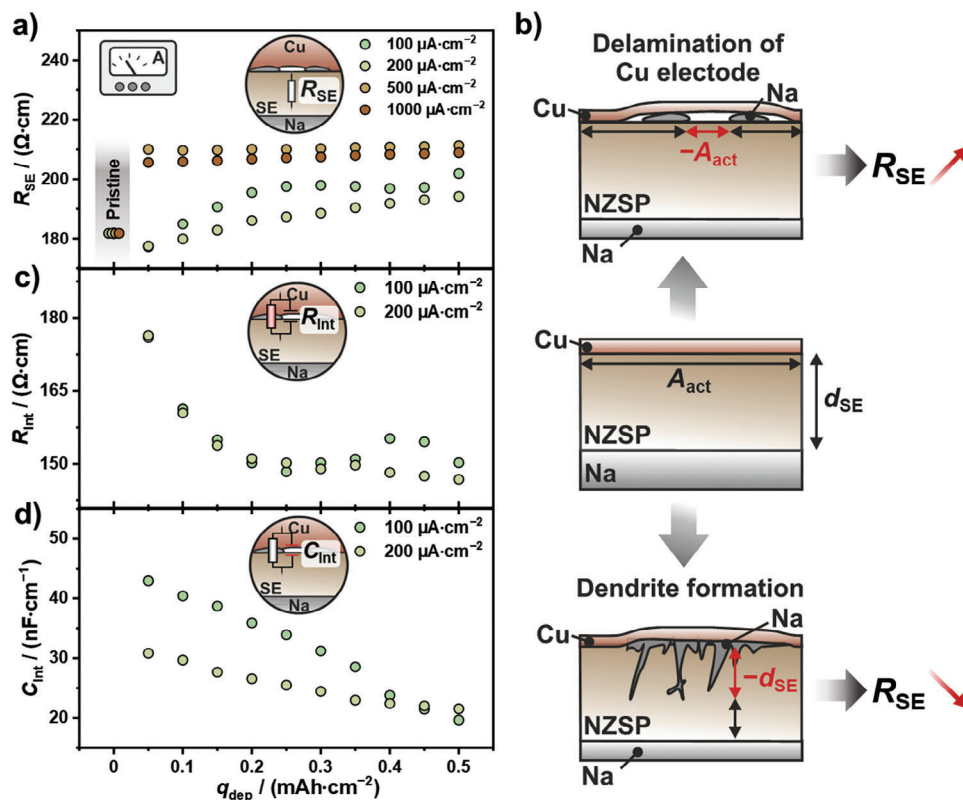
Figure 3. a) Evolution of the solid electrolyte resistance R_{SE} (sum of R_{Bulk} and R_{GB}) during cathodic deposition of sodium at the Cu|NZSP interface for various current densities. Deposition was carried out at $p = 2$ MPa and $T = 25$ °C. Impedance data were fitted using the equivalent circuit models depicted in Figure 2 and normalized with respect to the cell constant. Due to the normalization to the cell constant, all pristine cells have the same R_{SE}. For a better overview, the R_{SE} of the pristine cells were slightly shifted and highlighted in gray. b) Scheme illustrating the influence of delaminating copper from NZSP (upper part) and dendrite formation (bottom part) on R_{SE} during cathodic deposition. The formation of an interfacial gap leads to a reduction in the electrode area A_{act} actively involved in transport in the frequency range of the grain boundary transport process, and thus to an increase of R_{SE}. In contrast, the distance between opposing electrodes decreases on average when sodium penetrates the SE. This is similar to reducing the effective thickness of the SE, resulting in a decrease of R_{SE}. c) Evolution of interface-related resistance R_{Int} and d) capacity C_{Int} at various j_{app}. The respective errors resulting from the fitting are shown in Figure S3 (Supporting Information).

a strong polarization in the low-frequency range. The high-frequency impedance contribution corresponds to the transport across grain boundaries (GB) and the low-frequency polarization originates from the ion blocking behavior of the copper electrode. The bulk impedance of NZSP is not captured in the measured frequency range and no contribution is observed with respect to the charge transfer at the NZSP|Na$_{id}$ interface.[47]

Independent of the current density, after the first sodium deposition interval at the working electrode (copper electrode), the interface polarization turns into a non-blocking behavior with a small tail in the low-frequency range. The non-blocking behavior indicates the formation of a sodium electrode. The small tail in the low-frequency range is frequently observed at metal|SE interfaces and is probably due to diffusion processes of the metal at the interface.[43] However, the real origin is not yet clarified so far. A second semicircle in the mid-frequency range in the Nyquist plot appears at low j_{app} (100 and 200 µA•cm^{-2}), while no contributions can be resolved at higher j_{app}. According to the distribution of relaxation times analysis, very weak signals are observed for long relaxation times at 500 µA•cm^{-2}, whereas no signals are present at 1000 µA•cm^{-2}, as shown in Figure S2 (Supporting Information). The second semicircle in the Nyquist plot

can be assigned to the Cu|NZSP interface and arises due to the current constriction phenomenon. As no additional interface-related impedance contribution is present at high j_{app}, such electrodes can be considered as a quasi-reference electrode, since charge transfer and SEI formation are negligible at the Na|NZSP interface.[36]

With progressing sodium deposition changes in the high- and mid-frequency range are observed, which are more pronounced at lower j_{app}. To analyze the evolution of the individual contributions in more detail, the impedance data were fitted using the equivalent circuit inserted in Figure 2. First, the evolution of the SE impedance contribution (high-frequency region) during sodium deposition is analyzed in more detail, that is, the total resistance R_{SE}, which is the sum of R_{Bulk} and R_{GB}, shown in **Figure 3**a. It should be noted that the direct comparison of R_{SE} of the pristine cell ($q_{dep} = 0$ mAh•cm^{-2}) and after the first deposition interval ($q_{dep} = 0.05$ mAh•cm^{-2}) is hampered because different equivalent circuits are used for fitting to account for the transition from blocking to non-blocking behavior of the working electrode. Small deviations in determining R_{SE} occur if the fitting model is altered, resulting in a small offset. We could compensate this difference numerically, as R_{SE} should of course not depend

on the fit model, but we prefer not to modify the data analysis in this way.

As sodium deposition progresses, a slight increase of R_{SE}, especially at lower j_{app}, is observed for the measurement series indicating an increase of the cell constant. A similar trend is also deduced from the distribution of relaxation times analysis shown in Figure S2 (Supporting Information). The increase of R_{SE} can be attributed to delamination of the copper electrode and the NZSP due to vertical growth of sodium, resulting in gaps at the interface.[31] Above a certain gap height and width, they are no longer dielectrically shorted even in the frequency range of the grain boundary transport process.[48] As shown schematically in Figure 3b, this reduces the electrode area that is actively involved in transport and thus increases the cell constant. At higher j_{app}, the impact of gap formation on R_{SE} is less pronounced, indicating more uniform deposition of sodium.

Based on the evolution of R_{SE}, detrimental dendrite growth during deposition is unlikely. As shown in Figure 3b, metal infiltration into the SE would lead on average to a reduction in cell thickness and thus to a reduction of the cell constant. This would lead to a decrease of R_{SE} as it was observed in the case of the lithium plating at a Cu|LLZO interface.[29] However, it cannot be completely ruled out that dendrites are formed in this work, since dendrite growth and gap formation have an opposing effect on the evolution of R_{SE}. Therefore, it is possible that dendrites form but they cannot be identified from R_{SE} because the evolution of R_{SE} seems to be dominated by the gap formation.

Figure 3c shows the evolution of R_{Int} at 100 and 200 µA•cm^{-2} determined based on the given equivalent circuit depicted in Figure 2. No clearly separated interface-related contribution can be identified in the Nyquist plots and distribution of relaxation time analysis (Figure S2, Supporting Information) for 500 and 1000 µA•cm^{-2}. To properly fit the impedance data, the equivalent circuit has been changed from R-RQ-RQ to R-RQ for these current densities. Accordingly, no interface-related contribution (R_{Int} and C_{Int}) is gained from the fitting and shown in the Figure 3.

At low current densities, only slight changes of R_{Int} are observed, limited to the first two deposition cycles. This suggests that the interfacial contact area between sodium and NZSP is already defined after the first sodium deposition cycles and does not change significantly with longer deposition time. As systematically investigated by Fleig et al. and Eckhardt et al., the constriction resistance depends strongly on the contact area as well as its spatial distribution at the interface.[45,46,49] Accordingly, R_{Int} decreases with increasing contact area or with finer distribution of the contact spots. Thus, it is challenging to derive the contact area directly from R_{Int}. A finer spatial distribution of contact could be achieved, for example, by the formation of new sodium nuclei at the Cu|NZSP interface during the deposition. However, after the initial nucleation, the formation of new sodium nuclei at the Cu|NZSP interface is unlikely because η_{growth} is usually smaller than η_{nuc}. In contrast, an increase in the contact area can be achieved, for example, by sodium deposition on the surface of existing sodium nuclei or by plastic flow of the already deposited sodium. As the applied stack pressure (2 MPa) is higher than the yield strength of polycrystalline bulk sodium ($\sigma_{Na} \approx 0.2$–0.3 MPa), plastic flow of sodium is likely.[31,50] If the contact area is enlarged by plastic flow of sodium, no change of R_{Int} would be expected when the stack pressure is below its yield strength. As can be
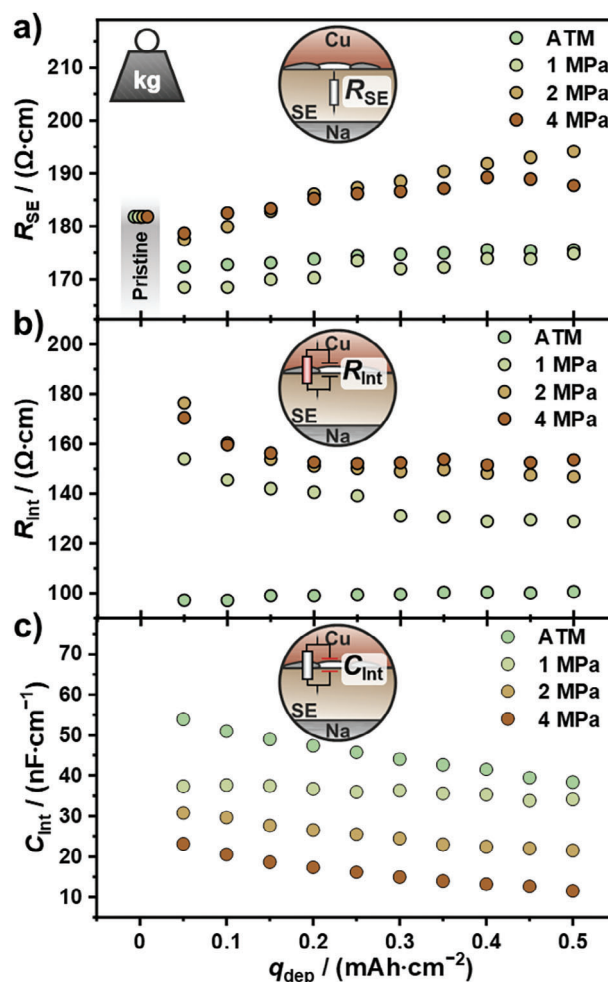
Figure 4. Evolution of solid electrolyte resistance R_{SE} (sum of R_{Bulk} and R_{GB}), interface-related resistance R_{Int}, and interface-related capacity C_{Int} at different stack pressures. Deposition was carried out at $j_{app} = 200$ µA•cm^{-2} and $T = 25$ °C. Impedance data were fitted using the equivalent circuit given in Figure S4 (Supporting Information) and normalized to the cell constants. Due to the normalization to the cell constant, all pristine cells have the same R_{SE}. For a better overview, the R_{SE} of the pristine cells were slightly shifted and highlighted in gray. Independent of the stack pressure, R_{SE} increases slightly as deposition progresses. R_{Int} initially decreases when stack pressure is applied, while it remains unchanged at atmospheric pressure. C_{Int} decreases slightly during the deposition of all measurements. The errors bars of the fitting are presented in Figure S5 (Supporting Information).

seen in **Figure 4**, R_{Int} remains constant during deposition when no stack pressure is applied. This supports our conclusion that the decrease of R_{Int} and thus an increase of the contact area is due to plastic flow of sodium. A more detailed discussion of the influence of stack pressure on the evolution of R_{Int} is given in Section 2.2.2.

The direct current resistances R_{DC} (sum of R_{SE} and R_{Int}) of the cells provide further information about the interface morphology. In a first approximation R_{DC} is inversely proportional to the contact area. This relationship suggests that the lower the R_{DC}, the larger the contact area. Consequently, a larger contact area

**ADVANCED
SCIENCE NEWS**

www.advancedsciencenews.com

**ADVANCED
ENERGY
MATERIALS**

www.advenergymat.de

between sodium and NZSP is achieved at higher current densities (see Figure 2).

The interfacial capacity C_{Int} depends on the morphology of the interface, i.e., the contact area and the height of the formed gap.[44] Figure 3d shows the evolution of C_{Int}, which decreases for both current densities. The reduction of C_{Int} would mean an increase of the gap height if the contact area remains almost unchanged. This is consistent with the observed trend of R_{SE}, which indicates a decrease in the electrode area actively involved in transport due to gap formation. An increase in the gap distance between copper and NZSP may be caused by vertical sodium growth. According to the trend in Figure 3d, vertical growth would be more pronounced at lower j_{app}. We like to emphasize that only the trend of the individual contributions (R_{SE}, R_{Int}, C_{Int}) was considered and analyzed qualitatively. A quantitate evaluation is not meaningful as the changes of the individual contributions are very small. With respect to a formal error analysis, shown in Figure S3 (Supporting Information), a quantitative change of a contribution is in the range of the fitting error.

2.2.2. Stack Pressure Series

Analogous to impedance analysis for the current density series, the influence of stack pressure on sodium deposition is discussed based on the evolution of the impedance. **Figure 4** shows the evolution of R_{SE}, R_{Int}, and C_{Int} during sodium deposition at different stack pressures. The corresponding impedance spectra and underlying distribution functions are shown in Figure S4 (Supporting Information). Starting with the evolution of R_{SE}, a sharp decrease is observed after the first deposition step for all stack pressures that is probably due to the different equivalent circuit models used. With progressing sodium deposition, a significant increase of R_{SE} is only observed at 2 MPa within the range of uncertainty, as shown in Figure S5 (Supporting Information). However, according to the results of the previous and also the following section, an increase of R_{SE} and thus gap formation is also likely at other stack pressures.

The evolution of R_{Int} for the stack pressure series is shown in Figure 4b. The corresponding formal errors for R_{Int} are given in Figure S5 (Supporting Information). Starting with the evolution of R_{Int} at atmospheric pressure, R_{Int} remains unchanged throughout the sodium deposition process. This indicates that the interfacial contact area as well as its distribution does not change significantly during deposition. In contrast, R_{Int} decreases within the first deposition intervals and flattens afterward, when a stack pressure above 1 MPa is applied. The reduction of R_{Int} results from a rise in the contact area due to plastic flow of sodium, caused by the stack pressure, which exceeds the yield strength of polycrystalline bulk sodium ($\sigma_{Na} \approx$ 0.2–0.3 MPa).[50]

However, this raises the question of why no continuous flow and thus no continuous decrease of R_{Int} is observed during deposition, especially when the stack pressure is elevated up to 4 MPa. This can be explained by the following reasons: First, the yield strength and flow stress strongly depends on the temperature, strain-rate, and aspect ratio.[50,51] Especially, at low aspect ratios (height/length), like metal films, the flow stress is dras-

tically increased under compression.[51] Second, frictional and adhesive forces at the interfaces additionally result in a hydrostatic pressure and thus reduce the plastic deformation of alkali metals.[50,52]

With the initial lateral deformation of sodium, the contact area between Na|CC and Na|SE increases and thus also frictional and adhesive forces. Furthermore, the aspect ratio decreases with lateral deformation, reinforcing the trend and resulting in a significant increase in flow stress. Consequently, the lateral deformation slows down and does not continue to increase the electrode area even though the applied stack pressure exceeds the yield strength of the polycrystalline bulk sodium.[50] Therefore, we attribute the initial decrease of R_{Int} to an increase of the contact area by plastic flow of sodium. With increasing contact area the plastic flow is reduced by additional frictional and adhesive forces and thus R_{Int} remains unchanged.

The direct current resistance R_{DC} (shown in Figure S4 Supporting Information) slightly decreases with decreasing the stack pressure as the lowest interface contribution is obtained at atmospheric pressure. Similar to the current density series, only slight changes of the direct current resistance, and thus the contact area, can be observed after the first sodium deposition intervals. This suggest that the interfacial contact area is mainly determined by the nucleation process. Hence, the stack pressure might affect the nucleation process. However, whether the stack pressure influences the lateral distribution of nuclei or the nucleation process itself requires further characterization, which will be investigated in future studies.

Finally, the evolution the interface-related capacity C_{Int} is shown in Figure 4c. Independent of the stack pressure, C_{Int} continues to decrease with progressing electrodeposition, indicating that the gap height is increasing, and thus supporting the trend and interpretation of the evolution of R_{SE}.

Based on the impedance analysis, the current density appears to have a stronger impact on interfacial morphology and the coverage of sodium than the stack pressure. According to the classical nucleation theory for electrodeposition from liquid electrolytes, the critical nucleation radius decreases with increasing η_{nuc} and the areal nucleation density increases.[41] In the case of a solid|solid interface, the mechanical work during nucleation needs to be considered additionally.[26] For Li deposition at Cu|LiPON and Cu|LLZO interfaces, an increase in areal nuclei density was observed with increasing current density, although there were no large changes in η_{nuc}.[12,27] For verification of the trend obtained from the electrochemical characterization, the samples were examined by light and electron microscopy to visualize the sodium deposition.

2.3. Characterization of Copper Electrodes after Cathodic Deposition

2.3.1. Light Microscopy

In addition to electrochemical characterization, copper electrodes were imaged from the top by light microscopy after deposition of $q_{dep} = 0.5$ mAh•cm^{-2} (corresponding to a sodium layer thickness of 4.4 µm assuming homogeneous deposition over the entire copper electrode). **Figure 5** shows the optical images (upper
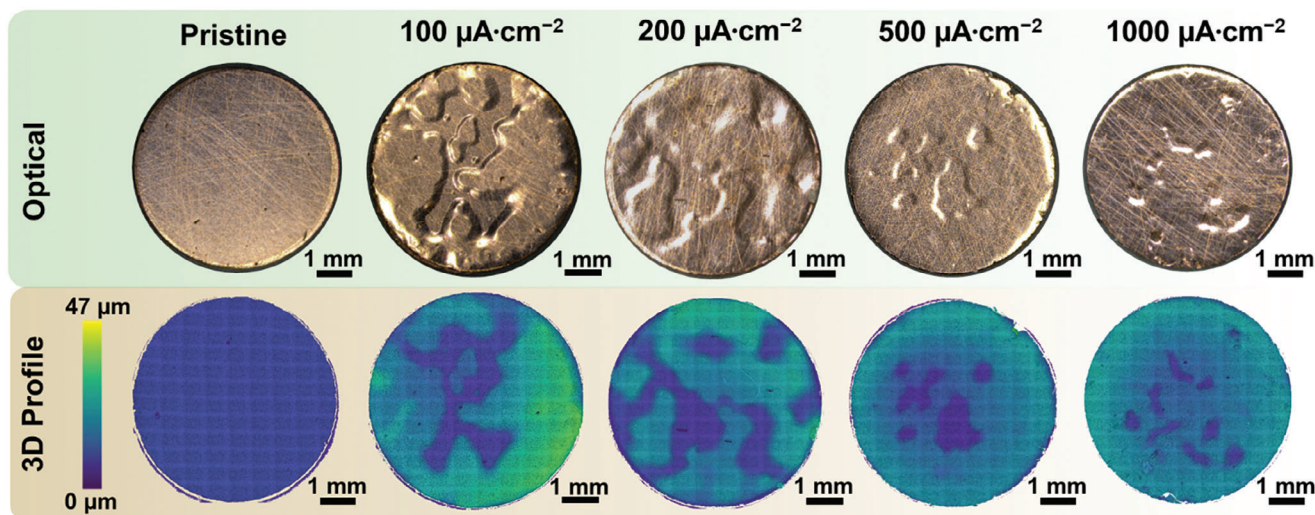
Figure 5. Optical microscopy images of copper electrode after cathodic deposition of $q_{dep} = 0.5$ mAh•cm^{-2} (upper row) at different current densities. The specimens were slightly tilted to improve the visibility of the topography in the optical images. In addition, the copper electrodes were imaged by confocal microscopy to generate a 3D representation (bottom row). Based on the optical and 3D confocal profiles, a more uniform coverage of the electrode is observed with increasing j_{app}.

row) and the corresponding 3D confocal microscopy profiles (bottom row) for the current density series. Starting from a smooth and flat pristine copper electrode, the optical images clearly show that the topography changes significantly, indicating inhomogeneous sodium growth underneath. It is also worth noting that no sodium whiskers grew through the copper electrode. The topographic changes of the copper electrode at different j_{app} are consistent with the trend of the impedance analysis. The 3D profiles reveal that the elevated areas of the copper electrode quantitatively increase as j_{app} increases, as shown in Figure 5 and Figure S6a (Supporting Information). Since the same amount of sodium was deposited in all measurements, stronger vertical growth must occur at smaller contact areas and vice versa. For instance, the absolute height difference at 100 µA•cm^{-2} is larger than for 1000 µA•cm^{-2}. Accordingly, the electrode area actively involved in transport is smaller at 100 µA•cm^{-2} than at 1000 µA•cm^{-2}, which supports our conclusion of better coverage at higher j_{app}.

For the stack pressure series, the elevated area of the copper electrode is smaller at atmospheric and low stack pressure (1 MPa) compared to high stack pressures (2 and 4 MPa), as can be seen in Figures S7 and S6b (Supporting Information). On the contrary, according to the direct current resistances R_{DC}, an opposite trend of the contact area is observed and thus is inconsistent with the 3D confocal microscopy profiles. This discrepancy is probably due to the mismatch between the elevated area and the actual contact area in the optical data, as described in Section 2.3.2. In general, the absolute height difference is higher at atmospheric pressure than with additional stack pressure. This is consistent with the trend of R_{Int}, since no plastic deformation and thus no lateral expansion of the sodium whiskers due to plastic flow is expected. Consequently, the height of an average whisker is higher for lower contact areas as the amount of sodium deposited remains constant. Similar behavior was also observed for the lithium deposition at the Cu|LLZO interface,

where vertical growth was less pronounced when a stack pressure was applied.[32]

2.3.2. Cross Sections of the Cu|Na|NZSP Interface

Since light microscopy only gives an overview of the surface of the copper electrode, additional cross-sections were prepared by FIB-SEM to visualize the deposited sodium in more detail. Multiple cross-sections per sample were prepared and linked to the position on the copper electrode in the 3D confocal microscopy profiles. **Figure 6** shows the cross-sections for the sample deposited at 200 µA•cm^{-2} and 2 MPa.

Starting with cross-section C1, a dense and uniform sodium layer with good contact to the NZSP and a thickness of 8.8 µm is found. The thickness is very well in line with the height difference obtained from the 3D profile at position C1. The thickness of ≈9 µm already indicates that there is no uniform sodium deposition over the entire copper electrode as the expected mean film thickness is 4.4 µm. Surprisingly, a discrepancy between the elevated area in the 3D profile and the sodium underneath is observed in the other cross-sections (C2-C4), revealing that the elevated area is not equal to the contact area between sodium and NZSP. For instance, a mismatch can result from the formation of gaps, as shown at positions C3 and C4. This can be caused by island or whisker growth. When sodium grows, the copper electrode near the island/whisker can be raised if the electrode is locally not bonded properly to the NZSP.[31,32] Although the lifted area in the 3D profiles does not correspond to the real contact area, it can provide information on the distribution of deposited sodium underneath the copper electrode.

The observation of large gaps supports the results of our impedance analysis given in Section 2.2. The increase in R_{SE} during deposition is associated with a reduction of the electrode area actively involved in transport, even at high frequencies, leading to

**ADVANCED
SCIENCE NEWS**

www.advancedsciencenews.com

**ADVANCED
ENERGY
MATERIALS**

www.advenergymat.de
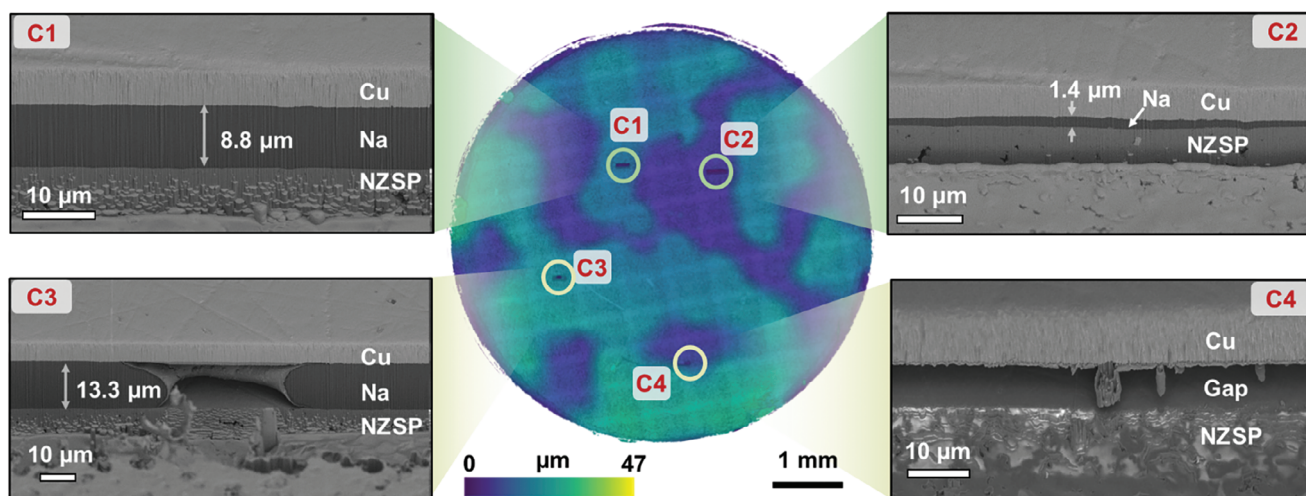
Figure 6. FIB-SEM cross-sections of selected spots on the copper electrode to visualize the sodium growth underneath. The positions are correlated with the corresponding 3D confocal microscopy profile as indicated by the labels C1-C4. The topography of the electrode in the 3D profile is indicated by the color bar shown on the bottom side. A total amount of sodium corresponding to $q_{dep} = 0.5$ mAh•cm^{-2} was deposited at $j_{app} = 200$ µA•cm^{-2}, $p = 2$ MPa, and $T = 25$ °C. Homogeneous deposition of a dense sodium layer with a homogeneous interfacial contact can be observed at position C1 and C2. Position C3 visualizes a region near the edge of a sodium island while at position C4 copper and NZSP is separated by a gap. The thickness of the deposited sodium varies between 1.4 and 13.3 µm.

a change in the cell constant. The formation of such gaps may be due to the preparation of the copper electrode, as they are less pronounced when a copper foil is laminated on a SE.[12,31,32] Lamination at elevated temperatures (<800 °C) and pressures (≈3 MPa) may improve the bonding between copper and SE.

Compared to the Cu|NZSP interface prepared by thermal evaporation, a small gap of ≈100 nm can be observed already in the pristine sample by Xe$^+$ FIB-SEM cross sections, as shown in Figure S8a–g (Supporting Information). When a TEM lamella of the stack prepared via Ga$^+$ FIB is prepared, an almost covering copper layer with small voids in the layer is obtained, as can be seen in Figure S8h,i (Supporting Information). It is unclear whether these voids were created by the FIB preparation or during the evaporation process. Therefore, it must be assumed that the copper electrode is not directly bonded to the solid electrolyte in some areas. Without direct bonding to the SE, there is no counterforce to push the copper electrode toward the SE when nearby vertical sodium growth lifts the electrode. Larger gaps have also been observed when the current collector is pressed only on a lithium SE, as in the case of Cu|Li$_6$PS$_5$Cl.[35]

Further cross-sections with the corresponding assignment to the respective 3D profile are shown in Figures S9–S11 (Supporting Information). Despite several cross-sections per sample, it is not possible to correlate the frequency of occurrence of growth features with the respective deposition parameters. This is because the cross sections provide only a local view. Therefore, only the generally observed phenomena of sodium deposition at the Cu|NZSP interface are described and summarized in **Figure 7**. Besides the formation of gaps, which occurs in all samples, mostly dense and uniform sodium layers with a conformal contact between sodium and NZSP are observed (Figure 7a,b). It is noteworthy that voids in the SE near the interface are not filled with sodium and no spallation of the SE is observed. The deposited sodium can adapt to the geometrical

conditions, even if the sodium layers are very thin (Figure 7c) or located in edge regions of the layer (Figure 7d). As shown in Figure 7e,f, besides a homogeneous deposition, the growth of small islands and whiskers can be observed leading to gap formation as discussed previously. Additionally, in the case of whisker growth no fracturing of the SE near the interface takes place.

Nevertheless, it cannot be ruled out that damage occurs near the Na|NZSP interface. As can clearly be seen in Figure 7g,h, parts of the SE are pulled out of the surface and voids in the SE are filled with sodium. Despite this spallation, a uniform sodium layer is obtained between the pulled-out SE and the remaining SE, which can be unambiguously concluded from the negative imprint in the remaining SE. The reason for the fracture has not been fully clarified. It cannot be excluded that sodium does nucleate inside the SE causing a high mechanical stress that leads to the formation of cracks. It is suggested that the root cause of the nucleation is related to the partial electronic conductivity of the SE.[53,54] In addition, the driving force for metal nucleation inside the SE needs to be considered.[7] Hence, nucleation can occur when the chemical potential of sodium inside the SE μ_{Na} exceeds the chemical potential of sodium metal μ^0_{Na}.[55] Such an "overshoot" of μ_{Na} can be caused by local ionic transport limitations or differences in transference number.[55,56] Moreover, to initiate sodium nucleation an overpotential has to be overcome that depends on the mechanical back stress of the respective SE.[57] For example, nucleation of sodium within the solid electrolyte has been observed for the sodium beta-alumina solid electrolyte.[56,58]

As the NZSP was polished prior to copper deposition, minor damages may have been induced, which led to local predetermined breaking points and further defects. These may act as preferred sites for nucleation and locally reduced fracture toughness of NZSP. However, the spallation of the SE appears to be very local, as can be seen in Figure 7g,d. Despite the presence of

**ADVANCED
SCIENCE NEWS**

www.advancedsciencenews.com

**ADVANCED
ENERGY
MATERIALS**

www.advenergymat.de
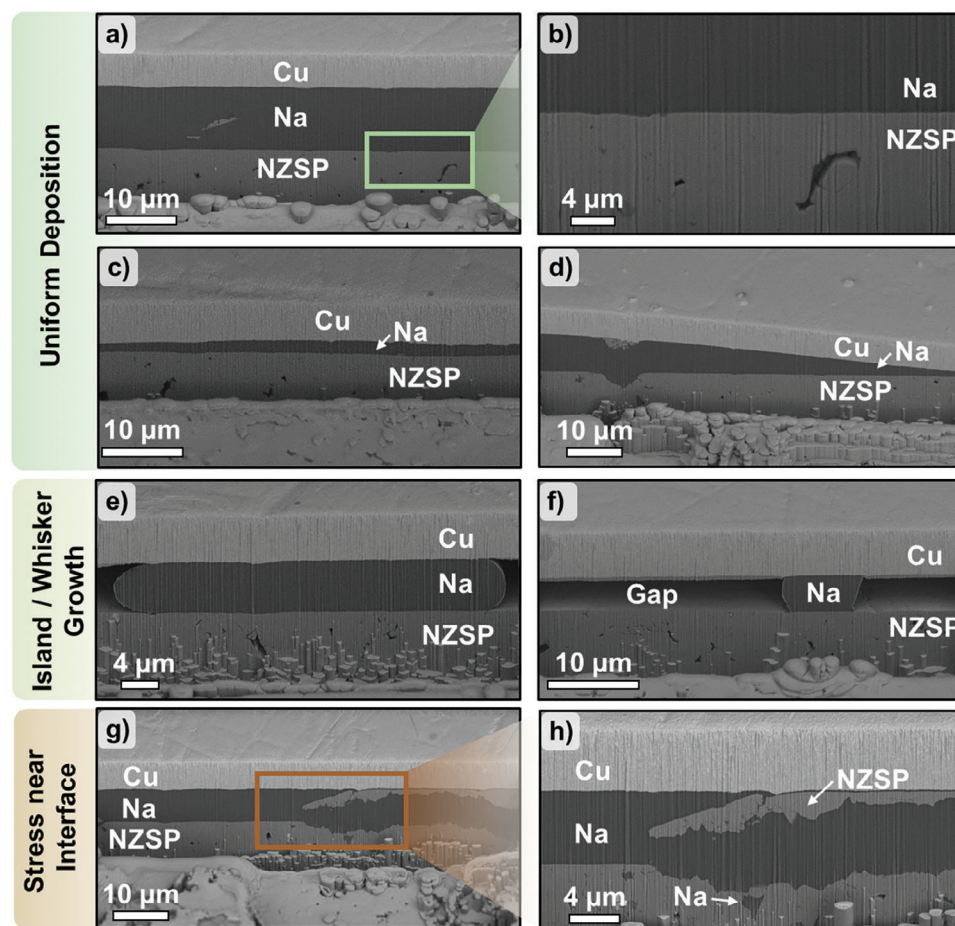
Figure 7. Compilation of FIB-SEM cross sections of differently observed phenomena during cathodic deposition of sodium at the Cu|NZSP interface. The formation of thick and uniform sodium layers with an optimal physical contact to the solid electrolyte are shown in (a) and (b). In addition, thin and wedge-shaped layers are observed in (c) and (d) with a proper contact to the copper electrode and the NZSP solid electrolyte. In contrast, island and whisker growth lead to gap formation between copper and NZSP as shown in (e) and (f). Moreover, NZSP grains near the interface break out and pores near the interface can be filled with sodium as identified in (g) and (h). The different morphologies and contrasts of NZSP result from the fact that both the crater wall (upper part) and the crater floor (lower part) are shown.

fractures, uniform deposition is again observed only a few micrometers next to it.

The cross sections generally show dense and uniform sodium deposition, which is required for sodium solid-state reservoir-free cells. Whisker growth, that is, out-of-plane or vertical growth, is not beneficial for the cycling of reservoir-free cells, as it leads to a reduction in the electrode area. However, it is not critical as no damage to the SE is observed in general. Clearly, spallation of the SE would lead to a degradation of the interface during cycling and may develop into a critical microstructural defect.

2.4. Characterization of Early Stages of Sodium Growth by In Situ Transmission Electron Microscopy (TEM)

For better understanding of the processes during early growth at the nanoscopic level, the sodium deposition at the Cu|NZSP interface was characterized by in situ TEM. A schematic representation of the experimental setup is depicted in Figure S12 (Supporting Information). Sodium growth at the interface was induced by applying a bias of 6.3 V and the morphological evolution has been recorded through time-series of high-angle annular dark-field scanning transmission electron microscopy images.

Starting from the pristine sample, besides a few close contact spots between copper and NZSP, several voids are present within the copper layer, as can be seen in **Figure 8**a. Moreover, a small crack in the SE is present near the interface, which is outlined with a green arrow in Figure 8b. The crack might be due to the polishing procedure of the SE or introduced by the ion milling.

During biasing, sodium nucleates at a close contact point shown in Figure 8c, highlighting the importance of physical contact between the copper and NZSP. With further biasing, a sodium whisker grows, which is highlighted by a brown dotted frame in Figure 8d. A polyhedral shape can be recognized. This might indicate a faceted single whisker, which is also observed in a second in situ TEM experiment, shown in FigureS13a,b (Supporting Information). We would like to note that the sample history of the second electron-transparent lamella differs from that of the first lamella, which is described in more detail in Section S5 (Supporting Information). However, such an oriented sodium

**ADVANCED
SCIENCE NEWS**

www.advancedsciencenews.com

**ADVANCED
ENERGY
MATERIALS**

www.advenergymat.de
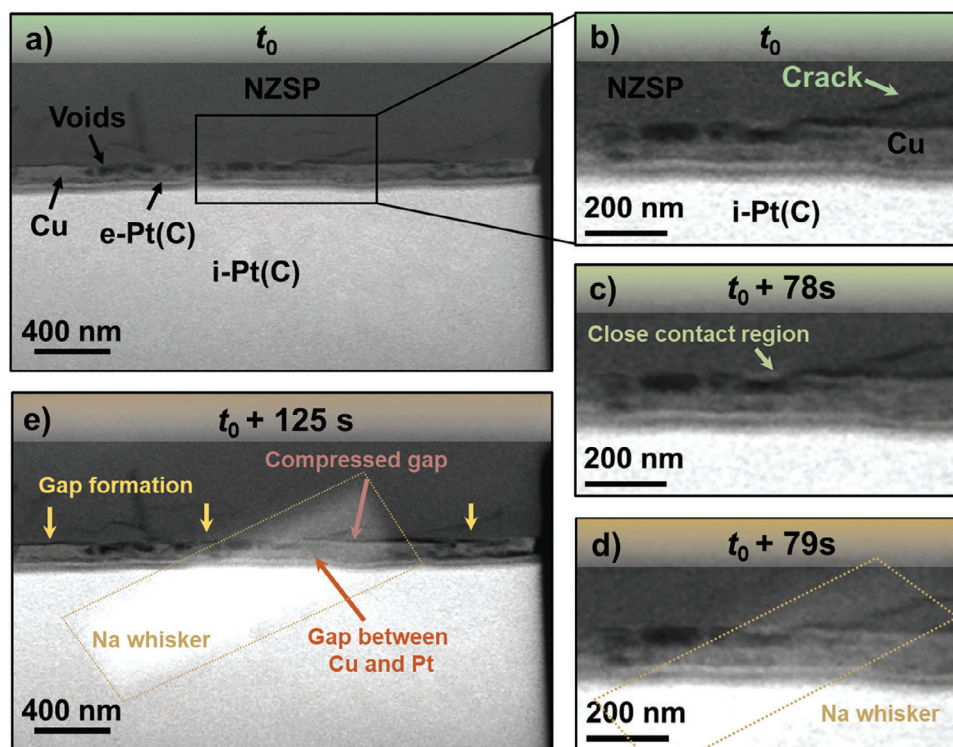
Figure 8. Time-resolved high-angle annular dark-field scanning transmission electron microscopy images of a Cu|NZSP interface during biasing. To initiate sodium deposition, the voltage was gradually increased and image acquisition was started when a voltage of 6.3 V was reached. This time is referred to as t_0. The pristine lamella is shown in (a) and (b). For processing of the lamella, a platinum protection layer was deposited via electron-beam (denoted as e-Pt(C)) followed by an ion-beam deposition referred to i-Pt(C). An initial crack near the Cu|NZSP interface is marked by a green arrow. c) After 78 s of polarization a sodium particle nucleates at a close contact spot highlighted with a light green arrow. During further polarization, the sodium particle grows into a polyhedral-shaped whisker. d) With progressing biasing, the formed whisker grows maintaining its shape (e). Furthermore, gap formation between the NZSP and copper layer (yellow arrows) as well as between the copper and platinum protection layer (orange arrow) is observed. Surprisingly, some gaps are also compressed as highlighted by a red arrow in (e).

growth has been observed previously in other TEM studies at (multiwall) carbon nanotube matrix.[59,60]

Moreover, the initial crack in Figure 8b (highlighted by the green arrow) does not further propagate during sodium nucleation and growth (Figure 8d). Therefore, existing cracks are not necessarily the starting point for further damage to the SE. On the contrary, damage to the SE due to the deposition cannot be completely ruled out. As shown in Figure S13c (Supporting Information), a crack forms in the SE near the interface. The formation of the crack may arise from mechanical stress generated by the deposition of sodium within the SE (see explanation in Section 2.3.2) or at the Cu|NZSP interface. Furthermore, the resulting crack can also serve as nucleation point. As can be seen in Figure S13d (Supporting Information), a second whisker is formed at the location of the previous crack. It is not clear whether the second whisker forms independently by plating inside the SE or whether a junction of the first whisker creates an electrical connection to the copper electrode and causes the formation.

The formation and growth of the sodium whisker also influences the copper current collector. In Figure 8e and Video S1 (Supporting information), gaps between copper and NZSP become enlarged or formed (indicated by yellow arrows), and compressed (indicated by red arrow). It is unclear if these phenomena are solely a result of the mechanical stress caused by the deposition of sodium as enlargement and compression are two opposite effects. Moreover, a minor expansion of the copper layer and detachment from the platinum protective layer (orange arrow) indicate additional factors that contribute to the observed changes in the electrode, beyond mechanical stress. However, small voids are also observed at the Cu|NZSP interface after sodium deposition, suggesting that sodium deposition bears the risk of delaminating copper from NZSP and agrees with the previous results (cf. Figure S13b, Supporting Information).

Note that we cannot exclude an influence of the specific lamella geometry in the operando experiments on the observed whisker growth. However, we assume that the faceted whisker growth of sodium is a general phenomenon that would also be observed in extended 3D samples.

3. Conclusions

In this work, we demonstrate the deposition of dense sodium layers with several microns thickness at the Cu|NZSP interface that are of comparable quality to reported electrodeposited lithium films.[31,32,35,61] To the best of our knowledge, there have not been reports on "anode-free" sodium deposition published yet. The electrodeposition and growth of sodium was studied at different

**ADVANCED
SCIENCE NEWS**

www.advancedsciencenews.com

**ADVANCED
ENERGY
MATERIALS**

www.advenergymat.de

current densities and stack pressures. Based on impedance analysis and optical microscopy, we conclude that a more homogeneous sodium distribution underneath the copper electrode can be achieved at higher current densities, whereas the stack pressure has a minor impact on the sodium distribution within the examined parameter window. We conclude that this interesting difference to lithium plating is due to the higher plasticity of sodium, which operates at room temperature quite close to its melting point.

FIB-SEM cross-sections show the deposition of dense and uniform sodium layers ideal for reservoir-free cells. Beside the layers, island, and whisker growth of sodium is also observed at the Cu|NZSP interface, leading to the formation of larger gaps due to incomplete physical contact between the copper electrode and the SE. The relevance of the initial physical contact is demonstrated by in situ TEM studies, as electrochemical sodium deposition only occurs at contact sites showing orientated growth of sodium whiskers. In addition, FIB-SEM cross-sections and in situ TEM characterizations reveal that sodium deposition can lead to crack formation and spallation of grains from the SE near the interface. However, based on the electrochemical impedance analysis, no detrimental dendrite formation is observed, even at higher current densities.

In order to obtain dense and homogeneous sodium layers, attention should be paid to the physical contact between the current collector and the SE, as well as to an adequate electrochemical deposition protocol. For example, ion beam sputtering of the copper layer could improve the interfacial contact between copper and NZSP compared to thermal evaporation technique due to the higher energy input of particles during deposition.[62] Moreover, pulse techniques with high current densities could be used to promote a homogeneous lateral sodium metal distribution but minimize damage to the solid electrolyte. We conclude that "reservoir-free" cell concepts can be realized for sodium solid-state batteries and hope to motivate further research in this field.

4. Experimental Section

Preparation of Reservoir-Free Cells: The NZSP solid electrolyte was synthesized via solution-assisted solid-state reaction (SA-SSR) as described elsewhere.[63] After sintering the NZSP pellets have a relative density of > 95%. For cell preparation, an ideally reversible sodium electrode was attached on one side of a NZSP pellet using a uniaxial load of 11 MPa for 1 min followed by additional isostatically pressing at 100 MPa for 15 min, as described previously.[36] The opposite side of the pellets was gradually polished with SiC grinding paper (Buehler Ltd., USA) starting from P400 up to P4000. A 5 µm copper layer was deposited on the polished surface by thermal evaporation in a home-built evaporation chamber.[29] During evaporation of copper the pressure inside the chamber was below 10^{-2} Pa. Before sealing of the Cu|NZSP|Na$_{id}$ assembly in an Ar-filled pouch bag, the copper electrode was covered by a nickel disc (thickness 1 mm) to ensure a homogeneous pressure distribution during electrochemical experiments. For measurements carried out at atmosphere pressures, the pouch bags were sealed under vacuum. The nickel disc was polished with an AutoMet 300 polishing machine (Buehler Ltd. USA) using a 1 µm polycrystalline diamond suspension (MetaDi Supreme, Buehler Ltd., USA). Preparation and assembling were conducted in an Ar-filled glovebox. A schematic illustration of the cell preparation, including the cell dimensions, is shown in Figure S1a (Supporting Information).

Electrochemical Characterization: Electrochemical measurements were conducted using a VMP-300 potentiostat (BioLogic, France) in a controlled temperature environment (LabEvent climate chamber, Weisstechnik, Germany) at 25 °C. The external load during cathodic deposition was maintained by an in-house build pressure frame equipped with an FC22 (TE Connectivity) force sensor.[40] For the characterization of the evolution of the Cu|NZSP interface, an alternating approach of chronopotentiometry and potentiostatic electrochemical impedance spectroscopy was used for cathodic deposition. A total amount of sodium corresponding to 0.5 mAh•cm^{-2} was cathodically deposited at the Cu|NZSP interface for all cells. Assuming an ideally uniform deposition of sodium across the entire copper electrode, a theoretical mean layer thickness of 4.4 µm would be expected. Impedance spectra were recorded after each deposition step of 0.05 mAh•cm^{-2} in a frequency range from 7 MHz to 100 Hz with a voltage amplitude of 10 mV.

Impedance data were analyzed using the Relaxis3 software package (rhd Instruments, Germany). The Kramers-Kronig test was used to check the spectra before fitting. Frequencies with relative residuals > 2% were not considered for fitting. The ionic blocking (polarization) behavior of the copper electrode in the pristine cells was fitted by a Q-element. The model used to fit the impedance data during cathodic sodium deposition is shown in the respective figures. All impedance data were normalized to the total conduction volume of NZSP using the fitted bulk and grain boundary resistance of the pristine cell. The specified errors of the determined resistances and capacitances were estimated by a formal error estimation based on the mathematical errors of the fit.

Distribution of relaxation times were analyzed by the software package Relaxis3 (rhd Instruments, Germany). The real and imaginary parts of the data set were considered for the evaluation. For solving the Tikhonov regularization problem, the second derivative of the distribution function $\gamma(\tau)$ was used. Calculations were performed with a shape factor of 0.5, a regularization parameter $\lambda = 10^{-6}$, and Gaussian basic functions.

3D Confocal Microscopy: After cathodic deposition, the copper electrodes were imaged by digital microscopy (Emspira 3, Leica Microsystems GmbH, Germany). The samples were slightly tilted to better visualize the topography of the copper electrodes. In addition, 3D confocal microscopy profiles of the copper electrodes were generated with an optical 3D profiler (S Neox confocal microscope, Sensofar, Spain) using the SensoSCAN 6.7 software package. The 3D profiles were processed and evaluated using the SensoVIEW 1.9.2 software package. The recorded 3D profiles were leveled by the other part of the copper electrode. Missing or unmeasured data points were reconstructed by interpolation (bicubic). Determination of the elevated area was conducted by the same software package.

Focused Ion Beam Scanning Electron Microscopy: Cross-sections of the Cu|Na|NZSP interface were prepared by FIB-SEM using a XEIA3 system (TESCAN GmbH, Czech Republic). The samples were transferred from a glovebox to a XEIA3 system under inert gas conditions using a Leica EM VCT500 transfer shuttle (Leica Microsystems GmbH, Germany). Prior to milling, the samples were cooled to a temperature of −143 K by liquid nitrogen, which was maintained during analysis. The cross-sections were milled with Xe$^+$ ions with an energy of 30 kV. Beam currents of 100–300 nA and 3–30 nA were used for milling and polishing. The cross sections were imaged by SEM using a low-energy back scattered electron detector (LE-BSE).

In Situ Transmission Electron Microscopy: For in situ TEM experiments, first a 120 nm thick copper film was deposited on a NZSP pellet by thermal evaporation. From this sample, a thick lamella with the Cu|NZSP interface was prepared using a Strata 400 S FIB microscope (FEI Company, USA) and attached to a copper TEM grid.[64] To protect the copper layer, a platinum protection layer was deposited by the electron and ion beam on the surface before milling. The final TEM lamella was obtained by thinning with a Ga$^+$ ion beam using an Auriga 60 CrossBeam FIB (Carl Zeiss NTS GmbH, Germany) following the cryogenic FIB processing routine for SE.[64]

TEM characterization was carried out using a probe-corrected Themis 300 system (Thermo Fisher Scientific, USA) operated at 300 kV and the in situ biasing was conducted using the scanning tunneling microscopy holder (ZEPtools Technology Company, PicoFemto double-tilt holder, China) inside the TEM. After establishing contact of the grounded tungsten tip with the platinum layer of the TEM lamella, a biasing voltage

of 4 and 6.3 V was applied between the copper TEM grid and the tungsten tip, respectively. The experimental setup is illustrated in Figure S12 (Supporting Information). Meanwhile, time-dependent series of high-angle annular dark-field scanning transmission electron microscopy images were acquired to record the morphological changes during biasing. The electron beam diameter was nominally 170 pm with nominal screen current of 100 pA.

Supporting Information

Supporting Information is available from the Wiley Online Library or from the author.

Conflict of Interest

The authors declare no conflict of interest.

Author Contributions

T.O. and T.F. designed the experiments. Q.M. and F.T prepared the solid electrolyte. T.O. prepared all cell and performed impedance analysis and cross sections experiments. T.O. and J.K.E. interpreted impedance analysis. Z.D. performed TEM sample preparation and characterization. T.O., Z.D., and C.K. interpreted TEM analysis. T.O., M.R., and J.J. wrote the manuscript. All authors discussed the results and contributed to the preparation of the manuscript.

Data Availability Statement

The data that support the findings of this study are available under DOI 10.5281/zenodo.10117406.

[1] J. Janek, W. G. Zeier, *Nat. Energy* **2023**, *8*, 230.
[2] C. Zhao, L. Liu, X. Qi, Y. Lu, F. Wu, J. Zhao, Y. Yu, Y.-S. Hu, L. Chen, *Adv. Energy Mater.* **2018**, *8*, 1703012.
[3] A. Banerjee, K. H. Park, J. W. Heo, Y. J. Nam, C. K. Moon, S. M. Oh, S.-T. Hong, Y. S. Jung, *Angew. Chem., Int. Ed.* **2016**, *55*, 9634.
[4] L. Zhou, J. D Bazak, B. Singh, C. Li, A. Assoud, N. M. Washton, V. Murugesan, L. F. Nazar, *Angew. Chem., Int. Ed.* **2023**, *62*, e202300404.
[5] M. D. Slater, D. Kim, E. Lee, C. S. Johnson, *Adv. Funct. Mater.* **2013**, *23*, 947.
[6] B. Xiao, T. Rojo, X. Li, *ChemSusChem* **2019**, *12*, 133.
[7] T. Krauskopf, F. H. Richter, W. G. Zeier, J. Janek, *Chem. Rev.* **2020**, *120*, 7745.
[8] Z. Lu, H. Yang, Q.-H. Yang, P. He, H. Zhou, *Angew. Chem., Int. Ed.* **2022**, *61*, e202200410.
[9] C. Heubner, S. Maletti, H. Auer, J. Hüttl, K. Voigt, O. Lohrberg, K. Nikolowski, M. Partsch, A. Michaelis, *Adv. Funct. Mater.* **2021**, *31*, 2106608.
[10] Q. Ni, Y. Yang, H. Du, H. Deng, J. Lin, L. Lin, M. Yuan, Z. Sun, G. Sun, *Batteries* **2022**, *8*, 272.
[11] O. Lohrberg, K. Voigt, S. Maletti, H. Auer, K. Nikolowski, C. Heubner, A. Michaelis, *Adv. Funct. Mater.* **2023**, *33*, 2214891.
[12] T. Fuchs, J. Becker, C. G. Haslam, C. Lerch, J. Sakamoto, F. H. Richter, J. Janek, *Adv. Energy Mater.* **2023**, *13*, 2203174.
[13] A. Willow, H. E. M. Hussein, S. Vajirakaphan, A. Chasri, S. Margadonna, *Front. Energy Res.* **2022**, *10*, 825.
[14] F. Mazzali, M. W. Orzech, A. Adomkevicius, A. Pisanu, L. Malavasi, D. Deganello, S. Margadonna, *ACS Appl. Energy Mater.* **2019**, *2*, 344.
[15] C. Wang, Y. Zheng, Z.-N. Chen, R. Zhang, W. He, K. Li, S. Yan, J. Cui, X. Fang, J. Yan, G. Xu, D. Peng, B. Ren, N. Zheng, *Adv. Energy Mater.* **2023**, *13*, 4.
[16] H. Li, H. Zhang, F. Wu, M. Zarrabeitia, D. Geiger, U. Kaiser, A. Varzi, S. Passerini, *Adv. Energy Mater.* **2022**, *12*, 2202293.
[17] B. Ma, Y. Lee, P. Bai, *Adv. Sci.* **2021**, *8*, 2005006.
[18] A. P. Cohn, N. Muralidharan, R. Carter, K. Share, C. L. Pint, *Nano Lett* **2017**, *17*, 1296.
[19] M. Tanwar, H. K. Bezabh, S. Basu, W.-N. Su, B.-J. Hwang, *ACS Appl. Mater. Inter.* **2019**, *11*, 39746.
[20] J. Seok, J.-H. Hyun, A. Jin, J. H. Um, H. D. Abruña, S.-H. Yu, *ACS Appl. Mater. Inter.* **2022**, *14*, 10438.
[21] R. Cao, K. Mishra, X. Li, J. Qian, M. H. Engelhard, M. E. Bowden, K. S. Han, K. T. Mueller, W. A. Henderson, J.-G. Zhang, *Nano Energy* **2016**, *30*, 825.
[22] X. Wang, C. Zhang, M. Sawczyk, J. Sun, Q. Yuan, F. Chen, T. C. Mendes, P. C. Howlett, C. Fu, Y. Wang, X. Tan, D. J. Searles, P. Král, C. J. Hawker, A. K. Whittaker, M. Forsyth, *Nat. Mater.* **2022**, *21*, 1057.
[23] A. Spangenberg, J. Fleig, J. Maier, *Adv. Mater.* **2001**, *13*, 1466.
[24] K. Peppler, J. Janek, *Solid State Ionics* **2006**, *177*, 1643.
[25] K. Peppler, M. Pölleth, S. Meiss, M. Rohnke, J. Janek, *Z. Phys. Chem.* **2006**, *220*, 1507.
[26] M. Motoyama, M. Ejiri, Y. Iriyama, *J. Electrochem. Soc.* **2015**, *162*, A7067.
[27] M. Motoyama, M. Hirota, T. Yamamoto, Y. Iriyama, *ACS App. Mater. Inter.* **2020**, *12*, 38045.
[28] M. Motoyama, M. Ejiri, T. Yamamoto, Y. Iriyama, *J. Electrochem. Soc.* **2018**, *165*, A1338.
[29] T. Krauskopf, R. Dippel, H. Hartmann, K. Peppler, B. Mogwitz, F. H. Richter, W. G. Zeier, J. Janek, *Joule* **2019**, *3*, 2030.
[30] S. Kim, C. Jung, H. Kim, K. E. Thomas-Alyea, G. Yoon, B. Kim, M. E. Badding, Z. Song, J. Chang, J. Kim, D. Im, K. Kang, *Adv. Energy Mater.* **2020**, *10*, 1903993.
[31] M. J. Wang, E. Carmona, A. Gupta, P. Albertus, J. Sakamoto, *Nat. Commun.* **2020**, *11*, 5201.
[32] E. Kazyak, M. J. Wang, K. Lee, S. Yadavalli, A. J. Sanchez, M. D. Thouless, J. Sakamoto, N. P. Dasgupta, *Matter* **2022**, *5*, 3912.
[33] B. J. Neudecker, N. J. Dudney, J. B. Bates, *J. Electrochem. Soc.* **2000**, *147*, 517.
[34] Y.-G. Lee, S. Fujiki, C. Jung, N. Suzuki, N. Yashiro, R. Omoda, D.-S. Ko, T. Shiratsuchi, T. Sugimoto, S. Ryu, J. H. Ku, T. Watanabe, Y. Park, Y. Aihara, D. Im, I. T. Han, *Nat. Energy* **2020**, *5*, 299.
[35] J. A. Lewis, S. E. Sandoval, Y. Liu, D. L. Nelson, S. G. Yoon, R. Wang, Y. Zhao, M. Tian, P. Shevchenko, E. Martínez-Pañeda, M. T. Mcdowell, *Adv. Energy Mater.* **2023**, *13*, 2204186.

[36] T. Ortmann, S. Burkhardt, J. K. Eckhardt, T. Fuchs, Z. Ding, J. Sann, M. Rohnke, Q. Ma, F. Tietz, D. Fattakhova-Rohlfing, C. Kübel, O. Guillon, C. Heiliger, J. Janek, *Adv. Energy Mater.* **2023**, *13*, 2202712.

[37] J. A. S. Oh, Y. Wang, Q. Zeng, J. Sun, Q. Sun, M. Goh, B. Chua, K. Zeng, L. Lu, *J. Colloid Interf. Sci.* **2021**, *601*, 418.

[38] E. Quérel, I. D. Seymour, A. Cavallaro, Q. Ma, F. Tietz, A. Aguadero, *J. Phys. Energy* **2021**, *3*, 044007.

[39] E. Quérel, N. J. Williams, I. D. Seymour, S. J. Skinner, A. Aguadero, *Chem. Mater.* **2023**, *35*, 853.

[40] T. Krauskopf, H. Hartmann, W. G. Zeier, J. Janek, *ACS Appl. Mater. Inter.* **2019**, *11*, 14463.

[41] A. Pei, G. Zheng, F. Shi, Y. Li, Y. Cui, *Nano Lett.* **2017**, *17*, 1132.

[42] P. Xu, X. Li, M.-Y. Yan, H.-B. Ni, H.-H. Huang, X.-D. Lin, X.-Y. Liu, J.-M. Fan, M.-S. Zheng, R.-M. Yuan, Q.-F. Dong, *J. Mater. Chem. A* **2021**, *9*, 22892.

[43] J. T. S. Irvine, D. C. Sinclair, A. R. West, *Adv. Mater.* **1990**, *2*, 132.

[44] J. K. Eckhardt, T. Fuchs, S. Burkhardt, P. J. Klar, J. Janek, C. Heiliger, *ACS App. Mater. Inter.* **2022**, *14*, 42757.

[45] J. K. Eckhardt, T. Fuchs, S. Burkhardt, P. J. Klar, J. Janek, C. Heiliger, *Adv. Mater. Inter.* **2023**, *10*, 2202354.

[46] J. K. Eckhardt, P. J. Klar, J. Janek, C. Heiliger, *ACS Appl. Mater. Inter.* **2022**, *14*, 35545.

[47] S. Lunghammer, Q. Ma, D. Rettenwander, I. Hanzu, F. Tietz, H. M. R. Wilkening, *Chem. Phys. Lett.* **2018**, *701*, 147.

[48] D. K. Singh, T. Fuchs, C. Krempaszky, P. Schweitzer, C. Lerch, F. H. Richter, J. Janek, *Matter* **2023**, *6*, 1463.

[49] J. Fleig, J. Maier, *J. Am. Ceram. Soc.* **1999**, *82*, 3485.

[50] M. J. Wang, J.-Y. Chang, J. B. Wolfenstine, J. Sakamoto, *Materialia* **2020**, *12*, 100792.

[51] A. Masias, N. Felten, J. Sakamoto, *J. Mater. Res.* **2021**, *36*, 729.

[52] C. G. Haslam, J. B. Wolfenstine, J. Sakamoto, *J. Power Sources* **2022**, *520*, 230831.

[53] F. Aguesse, W. Manalastas, L. Buannic, J. M. Lopez Del Amo, G. Singh, A. Llordés, J. Kilner, *ACS Appl. Mater. Inter.* **2017**, *9*, 3808.

[54] F. Han, A. S. Westover, J. Yue, X. Fan, F. Wang, M. Chi, D. N. Leonard, N. J. Dudney, H. Wang, C. Wang, *Nat. Energy* **2019**, *4*, 187.

[55] Y. Dong, Z. Zhang, A. Alvarez, I.-W. Chen, *Acta Mater.* **2020**, *199*, 264.

[56] L. C. De Jonghe, *J. Electrochem. Soc.* **1982**, *129*, 752.

[57] R. Raj, J. Wolfenstine, *J. Power Sources* **2017**, *343*, 119.

[58] L. C. De Jonghe, L. Feldman, A. Beuchele, *J. Mater. Sci.* **1981**, *16*, 780.

[59] L. Geng, C. Zhao, J. Yan, C. Fu, X. Zhang, J. Yao, H. Sun, Y. Su, Q. Liu, L. Zhang, Y. Tang, F. Ding, J. Huang, *J. Mater. Chem. A* **2022**, *10*, 14875.

[60] Q. Liu, L. Zhang, H. Sun, L. Geng, Y. Li, Y. Tang, P. Jia, Z. Wang, Q. Dai, T. Shen, Y. Tang, T. Zhu, J. Huang, *ACS Energy Lett* **2020**, *5*, 2546.

[61] C. Haslam, J. Sakamoto, *J. Electrochem. Soc.* **2023**, *170*, 040524.

[62] M. Ohring, *The Materials Science of Thin Films*, Academic Press, Cambridge, Massachusetts, USA **2022**.

[63] Q. Ma, C.-L. Tsai, X.-K. Wei, M. Heggen, F. Tietz, J. T. S. Irvine, *J. Mater. Chem. A* **2019**, *7*, 7766.

[64] Z. Ding, Y. Tang, V. S. K. Chakravadhanula, Q. Ma, F. Tietz, Y. Dai, T. Scherer, C. Kübel, *Microscopy* **2023**, *74*, 326.

2302729 (14 of 14)